





Investigation of the correlation between optical and γ -ray flux variations in the blazar Ton 599

Bhoomika Rajput ^{1,2}★, Amit Kumar Mandal,³ Ashwani Pandey ⁴, C. S. Stalin,⁵
Walter Max-Moerbeck ¹ and Blesson Mathew ²

¹Departamento de Astronomía, Universidad de Chile, Camino El Observatorio 1515, Las Condes, Santiago 7570840, Chile

²Department of Physics, CHRIST (Deemed to be University), Hosur Road, Bangalore 560029, India

³Astronomy Program, Department of Physics and Astronomy, Seoul National University, Seoul 151-742, Republic of Korea

⁴Center for Theoretical Physics, Polish Academy of Sciences, Al. Lotników 32/46, PL-02-668 Warsaw, Poland

⁵Indian Institute of Astrophysics, Block II, Koramangala, Bangalore 560034, India

Accepted 2023 December 21. Received 2023 December 19; in original form 2023 September 13

ABSTRACT

The correlation between optical and γ -ray flux variations in blazars reveals a complex behaviour. In this study, we present our analysis of the connection between changes in optical and γ -ray emissions in the blazar Ton 599 over a span of approximately 15 yr, from 2008 August to 2023 March. Ton 599 reached its highest flux state across the entire electromagnetic spectrum during the second week of 2023 January. To investigate the connection between changes in optical and γ -ray flux, we have designated five specific time periods, labelled as epochs A, B, C, D, and E. During periods B, C, D, and E, the source exhibited optical flares, while it was in its quiescent state during period A. The γ -ray counterparts to these optical flares are present during periods B, C, and E; however, during period D, the γ -ray counterpart is either weak or absent. We conducted a broad-band spectral energy distribution (SED) fitting by employing a one-zone leptonic emission model for these epochs. The SED analysis unveiled that the optical–ultraviolet emission primarily emanated from the accretion disc in quiescent period A, whereas synchrotron radiation from the jet dominated during periods B, C, D, and E. Diverse correlated patterns in the variations of optical and γ -ray emissions, like correlated optical and γ -ray flares, could be accounted for by changes in factors such as the magnetic field, bulk Lorentz factor, and electron density. On the other hand, an orphan optical flare could result from increased magnetic field and bulk Lorentz factor.

Key words: galaxies: active – galaxies: jets – galaxies: nuclei – gamma-rays: galaxies.

1 INTRODUCTION

Blazars, the peculiar category of active galactic nuclei (AGNs) known for emitting non-thermal variable radiation covering the whole range of the electromagnetic spectrum, are among the most luminous objects in the Universe (luminosity $\approx 10^{42}$ to 10^{48} erg s⁻¹). These objects emit relativistic jets that are oriented in the same direction as the observer’s line of sight (Antonucci 1993; Urry & Padovani 1995), resulting in strong Doppler boosting. They reside within elliptical galaxies (Urry et al. 2000) and their energy source is derived from the process of material accreting on to a supermassive black hole (10^6 to 10^{10} M_⊙; Shakura & Sunyaev 1973; Shaw et al. 2012).

Blazars are categorized into two groups: flat spectrum radio quasars (FSRQs) and BL Lacs. This classification relies on the rest-frame equivalent width (EW) of the emission lines observed in their optical spectra. FSRQs exhibit strong emission lines (EW > 5 Å), while BL Lacs exhibit either weak or no emission lines (EW < 5 Å; Stocke et al. 1991; Scarpa & Falomo 1997). The absence of broad emission lines in the optical spectra of BL Lac objects may be caused by Doppler-boosted non-thermal continuum, which could swamp out

the spectral emission lines (Blandford & Rees 1978). Additionally, the presence of EW > 5 Å observed in BL Lac objects might be the outcome of an especially low state of the beamed continuum (Vermeulen et al. 1995). Consequently, the EW by itself is not a reliable indicator of the difference between the two categories of blazars. Ghisellini et al. (2011) and Sbarrato et al. (2012) proposed a categorization scheme for FSRQs and BL Lacs that hinges on the luminosity of the broad-line region (BLR), which is measured in Eddington units. In accordance with this scheme, the luminosity of the BLR (L_{BLR}) to the Eddington luminosity ratio for FSRQs is greater than 5×10^{-4} , while it is less than 5×10^{-4} for BL Lacs.

The broad-band spectral energy distribution (SED) of blazars has a two-hump structure, where one hump peaks at lower energies in the optical/infrared (IR)/X-ray bands and the second hump peaks at higher energies in the MeV/GeV bands (Fossati et al. 1998; Mao et al. 2016). The low-energy emission is attributed to the synchrotron emission process of the relativistic electrons in the jets (Urry & Mushotzky 1982; Impey & Neugebauer 1988). Padovani & Giommi (1995) and Abdo et al. (2010c) proposed an alternative method of categorizing blazars by considering the position of the synchrotron peak frequency ($\nu_{\text{peak}}^{\text{syn}}$) in their SED. These classes include low-synchrotron peaked (LSP) blazars ($\nu_{\text{peak}}^{\text{syn}} < 10^{14}$ Hz),

* E-mail: bhoomikarjpt2@gmail.com

intermediate-synchrotron peaked blazars (10^{14} Hz $< \nu_{\text{peak}}^{\text{syn}} < 10^{15}$ Hz), and high-synchrotron peaked blazars (10^{15} Hz $< \nu_{\text{peak}}^{\text{syn}} < 10^{17}$ Hz). Most FSRQs are LSP blazars, while BL Lac sources exhibit all three blazar behaviours. Some BL Lacs are extremely high synchrotron peaked blazars (extreme blazars) with $\nu_{\text{peak}}^{\text{syn}} > 10^{17}$ Hz (Foffano et al. 2019).

It is renowned that the synchrotron emission process results in low-energy emission. However, the origin of the higher energy peak remains partially understood. To explain this, numerous models have been developed. Leptonic model often provides a satisfactory explanation for the observed broad-band SED of the majority of blazars. In the leptonic scenario, the high-energy emission is produced by the inverse Compton (IC) process (Abdo et al. 2010c). The seed photons that cause the IC process because of the scattering of the relativistic electron in the jets can originate from a variety of locations. These could originate from within the jets by synchrotron emission process (synchrotron self-Compton or SSC; Konigl 1981; Marscher & Gear 1985; Ghisellini & Maraschi 1989; Tramacere et al. 2009) or from outside the jets (external Compton or EC) mainly from the accretion disc (Boettcher, Mause & Schlickeiser 1997; Dermer & Schlickeiser 2002), from the BLR (Ghisellini & Madau 1996; Dermer et al. 2009), and from the dusty torus (Błażejowski et al. 2000; Sikora, Moderski & Madejski 2008).

In addition to the leptonic model, the high-energy peak in the broad-band SED of blazars can also be accounted for by the hadronic model (Böttcher et al. 2013). Hadronic model for blazar postulates that protons are accelerated to ultra-relativistic energies and dominate the high-energy emission through proton–synchrotron radiation (Aharonian 2000; Mücke et al. 2003) or photopion production via proton–proton or proton–photon interaction (Mannheim 1993), which results in the production of ultra-high-energy photons and neutrinos. The hybrid lepto-hadronic model has also been proposed in some cases to explain high-energy emission in blazar (Diltz & Böttcher 2016; Paliya et al. 2016; Cerruti et al. 2019).

In addition to the broad-band SED, the study of the temporal correlation between the two major components of the broad-band emission, i.e. optical and γ -ray emission, can give major insights into the high-energy emission in blazars. In the leptonic model of blazar emission, since the relativistic electrons in the jets are responsible for both the optical and γ -ray emission (Böttcher 2007), a close correlation between the optical and γ -ray flux changes is anticipated. The launch of the *Fermi* Gamma-ray Space Telescope¹ (referred to as *Fermi* hereafter; Atwood et al. 2009) in 2008 gave us unusual opportunity to characterize the γ -ray for a large number of sources (Abdollahi et al. 2020). To investigate the connection between the optical and γ -ray bands, *Fermi* data were combined with numerous ground-based optical and IR observations. Several studies have been conducted on this topic, yielding diverse conclusions. For example, correlations between optical and γ -ray changes, with or without lag, have been found in blazars (Bonning et al. 2009; Chatterjee et al. 2012; Liao et al. 2014; Lioudakis et al. 2018). These findings firmly support the leptonic model of blazar emission. However, many studies disfavour the one-zone leptonic model due to the absence of a correlation between changes in optical and γ -ray flux. In these studies, either γ -ray flares are present without their corresponding optical flares (orphan γ -ray flares; Dutka et al. 2013; Cohen et al. 2014; MacDonald et al. 2015; Rajput, Stalin & Sahayanathan 2020) or optical flares are present without their γ -ray counterparts (orphan optical flares;

Chatterjee et al. 2013; Rajput et al. 2019, 2020, and references therein).

The existing observations suggest that the correlation between variations in optical flux and γ -ray flux is intricate. In this work, we conducted a thorough examination over the long-term duration to understand the diverse behaviour between changes in optical and γ -ray flux through broad-band SED modelling in the blazar Ton 599. This blazar was recently observed at its brightest state (Garrappa & Valverd 2023; Prince 2023; Tripathi et al. 2023). The availability of multiwavelength data over the long-term period renders this source appropriate candidate for conducting study on the optical–GeV connection. Ton 599, also known as 4C +29.45, is named as 4FGL J1159.5+2914 in the fourth catalogue of *Fermi* Large Area Telescope (4FGL; Abdollahi et al. 2022). It is located at a redshift $z = 0.725$ (Hewett & Wild 2010), with RA = 179:882 641 and Dec. = 29:245 507. This source is classified as an FSRQ source and it falls under the category of LSP source (Abdo et al. 2010a). It displays high optical variability and exhibits strong polarization (Fan et al. 2006). In the γ -ray band, this source was first detected by the Energetic Gamma Ray Experiment Telescope (Thompson et al. 1995) and later by the *Fermi* (Abdo et al. 2010b). Moreover, this source was detected by VERITAS (Very Energetic Radiation Imaging Telescope Array System) in the very high energy (>100 GeV) band (Mukherjee & VERITAS Collaboration 2017). This source is observed with significant variability in the optical and γ -ray bands, as well as in other bands of the electromagnetic spectrum (Fan et al. 2006; Patel et al. 2018; Prince 2019; Rajput & Pandey 2021; Bhatta et al. 2023). In 2017, Ton 599 was detected in an unprecedented massive flaring state across the entire electromagnetic spectrum (Acosta Pulido et al. 2017; Carrasco et al. 2017; Cheung, Gasparrini & Buson 2017). The optical and GeV connection for this source during its 2017 outburst was investigated by Prince (2019), and optical and γ -ray emission regions are found to be co-spatial with the time lag of a few days. This source was modelled using a two-zone leptonic emission model during the same flare by Patel & Chitnis (2020), and it was found that the GeV emission was from EC process, where the seed photons originated from the dusty torus. The largest flare ever recorded by *Fermi* for this source in a period of around 15 yr occurred in 2023 January when Ton 599 was once again found to be flaring, with a flux value of $3.60 \pm 0.27 \times 10^{-6}$ ph cm⁻² s⁻¹. Here, we present the findings of a multiwavelength analysis performed on the blazar Ton 599 using data collected over a period of about 15 yr, from 2008 August to 2023 March. The main objective of this analysis is to determine any potential correlation between variations in the optical V -band flux and γ -ray flux and, as a result, putting constraints on the emission process in blazars. We provide the information about the data utilized in this work in Section 2. Section 3 provides a detail of the analysis, and Section 4 presents the findings and a discussion. The summary of the work is given in the final section.

2 MULTIWAVELENGTH DATA REDUCTION

To carry out a multiwavelength analysis of the source Ton 599, we used publicly accessible data in the γ -ray, X-ray, ultraviolet (UV), and optical bands that span around 15 yr, from 2008 August to 2023 March.

2.1 γ -ray data

We analysed about 15 yr of data collected from the Large Area Telescope (LAT) aboard the *Fermi*. The *Fermi*-LAT is a pair-

¹<https://fermi.gsfc.nasa.gov/ssc/data/access/lat/>

conversion telescope and has a very large effective area ($>8000 \text{ cm}^2$; Atwood et al. 2009). It usually operates in the scanning mode and scans the entire sky once every ~ 3 h covering an extensive spectral energy range from 20 MeV to TeV energies. For this study, we performed binned likelihood analysis by using the *Fermi*-LAT data in the energy range of 100 MeV to 300 GeV from 2008 August 8 to 2023 March 5, a period of approximately 15 yr (MJD 54686–60008). To analyse the *Fermi* data, we used the current version of FERMITOOLS 2.2.0. We used PASS 8 data where the photon-like events are categorized as ‘evclass = 128, evtype = 3’. All the events were chosen within a 10° circular region of interest centred on the source and a 90° zenith angle cut was made to eliminate background γ -rays from the Earth’s limb. After that, we generated a good time interval using the suggested criteria ‘(DATA QUAL > 0) && (LAT CONFIG == 1)’. For this analysis, we used the latest instrument response function ‘P8R3_SOURCE_V3’, Galactic diffuse emission model ‘gll_iem_v07’, and the extragalactic isotropic diffuse emission model ‘iso_P8R3_SOURCE_V3_v1’. Our source model includes all the point sources from the 4FGL catalogue that fall within 10° of the source, as well as the Galactic and the extragalactic isotropic diffuse emission components. The spectral shapes of all the sources are adopted from the 4FGL catalogue. For the sources lying between 0° and 5° , the spectral parameters are left free except the scaling factor and for the sources lying between 5° and 10° , all the spectral parameters are kept fixed to their 4FGL catalogue value. To determine the significance of the detection, we used the maximum likelihood (ML) test statistic, defined as $\text{TS} = 2\Delta \log(L)$, where L represents the likelihood function comparing models with and without a γ -ray point source at the source’s location. During the likelihood analysis, the sources with $\text{TS} < 25$, which corresponds to a 5σ detection (Mattox et al. 1996), were removed. This modified model is then employed for the analysis of the light curve and spectra. To generate the 1-d binned γ -ray light curve over the time period of interest, we regarded the source as detectable when the value of $\text{TS} > 9$, equivalent to a 3σ detection.

2.2 X-ray data

2.2.1 Swift-XRT data

The X-ray telescope (XRT), as detailed in Burrows et al. (2005), mounted on the *Swift* satellite (Gehrels et al. 2004), operates within the 0.3–10 keV energy range, observed Ton 599 concurrently with *Fermi*. The X-ray data utilized in this work were taken from the archives at High Energy Astrophysics Science Archive Research Center (HEASARC).² To analyse the data, we adhered the standard procedure given by the instrument pipeline. We used the data obtained only in the photon counting (PC) mode for the light curve and spectrum analysis. We analysed the data with the `xrtpipeline` task, utilizing the latest CALDB (calibration database) and response files provided in HEASOFT version 6.29. We employed the standard grade selection 0–12. To generate the energy spectra, the calibrated and cleaned event files were added. The source spectra were extracted from a circular area with a radius of 60 arcsec, positioned at the centre of the source, whereas the background spectra were extracted from a region with a radius of 80 arcsec, located away from the source. The exposure maps were combined using the `ximage` task, and the ancillary response files (ARFs) were created using the `xrtmkarf` task. The corresponding response matrix files (RMFs) were obtained

²<https://heasarc.gsfc.nasa.gov/docs/archive.html>

from CALDB. The RMFs and ARFs were loaded into the `grppha` tool together with the source and background spectra in order to combine and group them. To perform the fitting of the final X-ray spectra within XSPEC (Arnaud 1996), we employed an absorbed simple power-law (PL) model with a Galactic neutral hydrogen column density $N_{\text{H}} = 1.63 \times 10^{20} \text{ cm}^{-2}$ (Dickey & Lockman 1990; Kalberla et al. 2005).

2.2.2 NuSTAR data

NuSTAR (Nuclear Spectroscopic Telescope Array), the first focusing hard XRT, was launched in 2012 June. It consists of two co-aligned X-ray detectors paired with their corresponding focal plane modules, called FPMA and FPMB, and it operates over a wide energy range from 3 to 79 keV (Harrison et al. 2013). *NuSTAR* recorded two observations of Ton 599 in 2019 May and 2021 June. For this study, we used one observation (ObsID 60463037004) during the 2021 flare of Ton 599 with an exposure time of 17.5 ks. The data were reduced using the *NuSTAR* Data Analysis Software package NUSTARDAS within the HEASOFT³ version 6.29. The calibrated and cleaned level 2 event files were produced using the `nupipeline` task and the CALDB version 20211202. We extracted the source and background spectra using a circular region of 30 arcsec with the `nuproducts` script. We grouped the spectra using `grppha` with at least 20 counts per bin and further processed it into XSPEC.

2.3 UV and optical data

We obtained the data in the UV and optical bands from *Swift*-UV/Optical telescope (*Swift*-UVOT). We analysed these data using the online tool.⁴ To generate the light curves in the UV and optical bands, the magnitudes obtained using the online tool were converted into fluxes using the zero-point method described in Breeveld et al. (2011) without correcting for galactic reddening. However, to examine the spectral characteristics of the source, the magnitudes were corrected for galactic extinction (A_λ), whose values were obtained from NED⁵ (NASA/IPAC Extragalactic Database). In addition to using optical data obtained from *Swift*-UVOT, we also incorporated optical V-band data from the ground-based survey ASAS-SN⁶ (All-Sky Automated Survey for Supernovae) and from the Steward Observatory (SO).⁷ The ASAS-SN ground-based survey operates with five stations positioned in both the Northern and Southern hemispheres. It has the capability to conduct daily observations of the entire visible sky, reaching a depth of $g = 18.5$ mag (Shappee et al. 2014; Kochanek et al. 2017). The SO, which is located in Arizona, employs the 2.3-m Bok Telescope and the 1.54-m Kuiper Telescope for photometric observations.

3 ANALYSIS

3.1 Multiwavelength light curves

We have generated multiwavelength light curves of the source Ton 599 for a period of about 15 yr from 2008 August 8 to 2023 March 5 (MJD 54686–60008). The multiwavelength light curves, which include 1-d binned γ -ray, X-ray (PC mode), UV, and optical light

³<http://heasarc.gsfc.nasa.gov/docs/nustar/analysis/>

⁴<https://www.ssdc.asi.it/cgi-bin/swiftuvarchiv>

⁵<https://ned.ipac.caltech.edu/>

⁶<https://asas-sn.osu.edu/>

⁷<http://james.as.arizona.edu/~psmith/Fermi/>

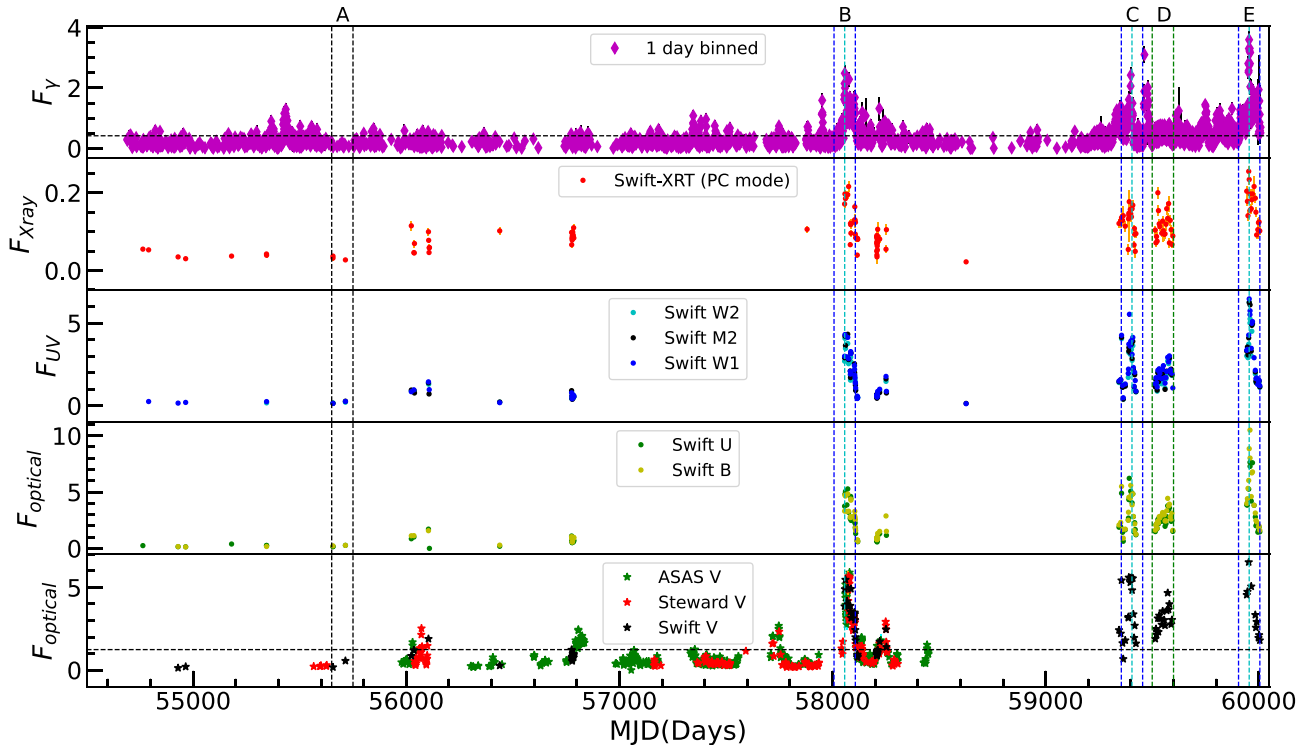


Figure 1. Multiwavelength light curves of the source Ton 599 for the period from MJD 54686 to MJD 60008. The top panel refers to the 1-d binned γ -ray (0.1–300 GeV) light curve, the second panel refers to the X-ray (0.3–10 keV) light curve, the third panel refers to the UV light curve, and the fourth and fifth panels refer to the optical light curves. The γ -ray fluxes are measured in the units of 10^{-6} ph cm^{-2} s^{-1} and the UV and optical fluxes are measured in the units of 10^{-11} erg cm^{-2} s^{-1} . The two vertical black dashed lines represent the quiescent epoch A. The vertical blue dashed lines refer to the flaring epochs B, C, and E, when both optical and γ -ray flares are present. The two vertical green dashed lines represent the flaring epoch D, when optical flare is present without its corresponding γ -ray counterpart. The peaks of optical and γ -ray flares are denoted by the vertical cyan dashed lines. The horizontal black dashed lines in the γ -ray and optical V-band light curves represent the average flux from 2008 August to 2023 March.

Table 1. Details of the epochs studied in this work for optical–GeV correlation and broad-band SED modelling. In this table, the optical flux values are in units of 10^{-11} erg cm^{-2} s^{-1} , and the γ -ray flux values are in units of 10^{-6} ph cm^{-2} s^{-1} .

Epoch	Status	Time period (MJD)		Calendar date		Average flux		Peak flux	
		Start	End	Start	End	Optical	γ	Optical	γ
A	Quiescent	55650	55750	2011-03-30	2011-07-08	0.37 ± 0.02	0.11 ± 0.02	0.56 ± 0.03	0.21 ± 0.09
B	Optical flare with γ -ray counterpart	58007	58107	2017-09-11	2017-12-20	3.89 ± 0.02	0.99 ± 0.02	5.47 ± 0.13	2.49 ± 0.28
C	Optical flare with γ -ray counterpart	59355	59455	2021-05-21	2021-08-29	3.62 ± 0.03	0.63 ± 0.02	5.60 ± 0.14	2.42 ± 0.28
D	Optical flare without γ -ray counterpart	59500	59600	2021-10-13	2022-01-21	3.03 ± 0.02	0.45 ± 0.01	4.67 ± 0.12	0.81 ± 0.05
E	Optical flare with γ -ray counterpart	59905	60005	2022-11-22	2023-03-02	5.55 ± 0.03	1.32 ± 0.03	10.30 ± 0.14	3.60 ± 0.27

curves, are shown in Fig. 1. From Fig. 1, it is conspicuous that Ton 599 has numerous quiescent and flaring stages during this period. We have identified specific time periods within this 15-yr duration. These include one quiescent period labelled as epoch A and four flaring periods (when an optical or γ -ray flare is present), marked as epochs B, C, D, and E. These quiescent and flaring epochs have a 100-d time span and flaring epochs are centred on the peak of either the γ -ray or optical light curves. The time periods of these epochs are given in Table 1. These epochs were chosen based on the following criteria: (1) The accessibility of multiwavelength data; (2) optical and γ -ray light-curve data during the quiescent phase should be below the average level; and (3) optical or γ -ray flare should gradually increase by more than two times from

the average level. The values of average optical and γ -ray fluxes are $1.24 \pm 0.003 \times 10^{-11}$ erg cm^{-2} s^{-1} and $0.42 \pm 0.003 \times 10^{-6}$ ph cm^{-2} s^{-1} , respectively, over the period from 2008 August to 2023 March. The average and peak values of optical and γ -ray flux for each epoch are given in Table 1. The details of each of the epochs are given below.

3.1.1 Epoch A (MJD 55650–55750)

The source was in a quiescent state in the γ -ray, X-ray, UV, and optical bands during this epoch. The multiwavelength light curve of this epoch is shown in the upper left panel of Fig. 2.

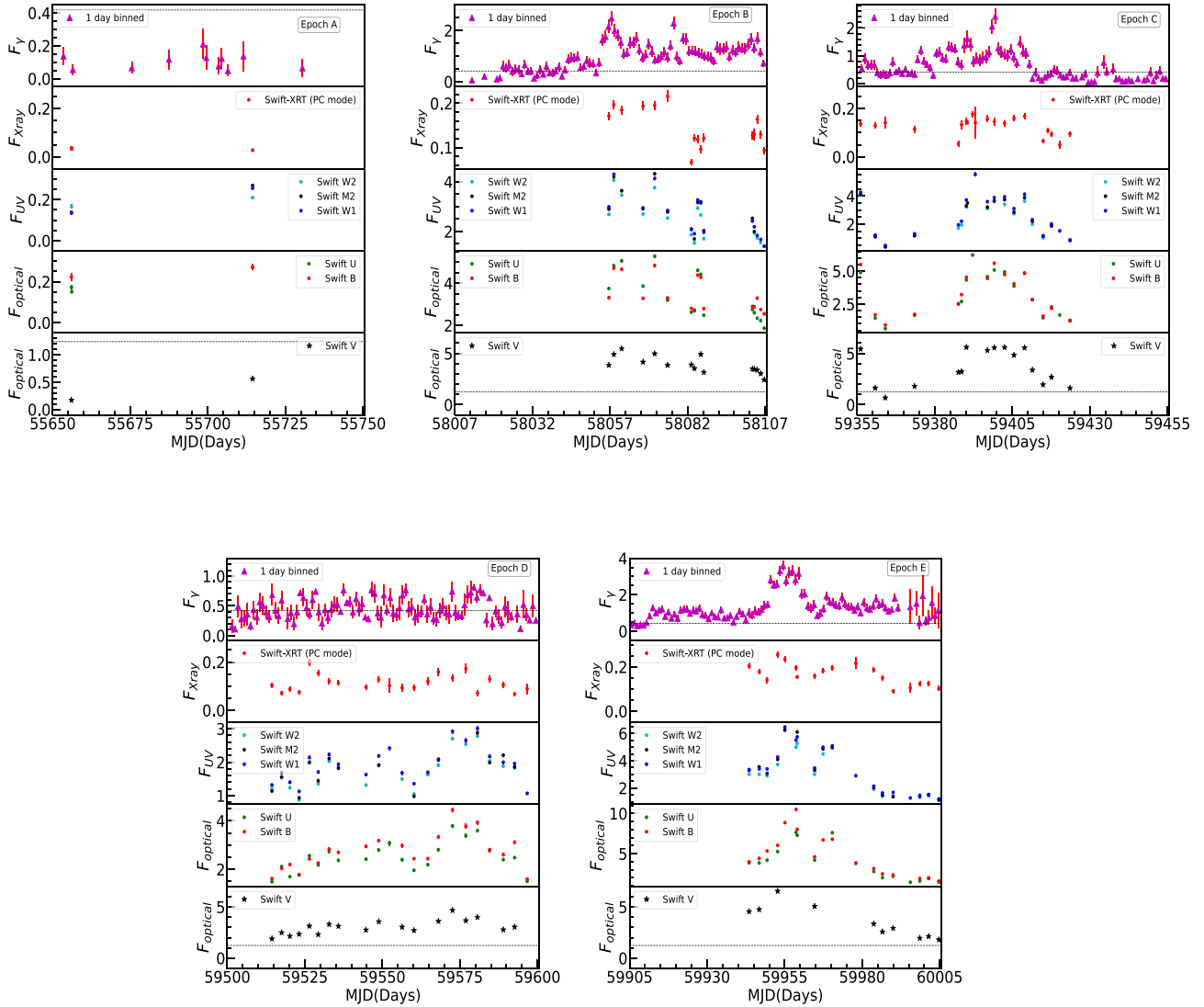


Figure 2. Multiwavelength light curves for the selected epochs A, B, C, D, and E. The light curves for epochs A, B, and C are displayed in the upper left, middle, and right panels, respectively. The bottom left and right panels represent the light curves for epochs D and E, respectively. The details of the panels are same as in Fig. 1.

3.1.2 Epoch B (MJD 58007–58107)

During this epoch, the source showed major variation in γ -ray flux. The γ -ray flux increased by about six times from the average level during this epoch. Along with the large changes in the γ -ray flux, changes in the X-ray, UV, and optical fluxes were also observed (refer to upper middle panel of Fig. 2). The optical flux also increased by nearly five times from the average level. During this epoch, two short-term intense γ -ray flares were observed superimposed on the large γ -ray flare at around MJD 58057 and MJD 58077. Visual inspection of Fig. 2 (upper middle panel) also gives the hint of corresponding short-term optical flare at around MJD 58057 but there is no hint of an optical flare at around MJD 58077 due to lack of data points. We deduce that during this time period, we noted the same patterns of flux variations in both the optical and GeV energy ranges.

3.1.3 Epoch C (MJD 59355–59455)

The source experienced a significant γ -ray flare during this epoch, this one being around six times greater than the γ -ray flux on average.

This substantial flaring event was subsequently accompanied by flares in the X-ray, UV, and optical bands. Notably, the optical flux experienced an increase of approximately five times compared to its average level. Thus, in this epoch too, we found that the variability pattern in the optical and γ -ray bands appeared to be correlated. The multiwavelength light curve for this epoch is shown in the upper right panel of Fig. 2.

3.1.4 Epoch D (MJD 59500–59600)

During this epoch, the γ -ray flux variations are moderate but the changes in the X-ray, UV, and optical flux are significant (see the lower left panel of Fig. 2). In comparison to the average flux level, the γ -ray flux increased by less than two times, whereas the optical flux increased by about four times compared to the average flux level. Since there was no clear large amplitude variation in the γ -ray light curve at this epoch, we can infer that in this epoch we observed an orphan optical flare.

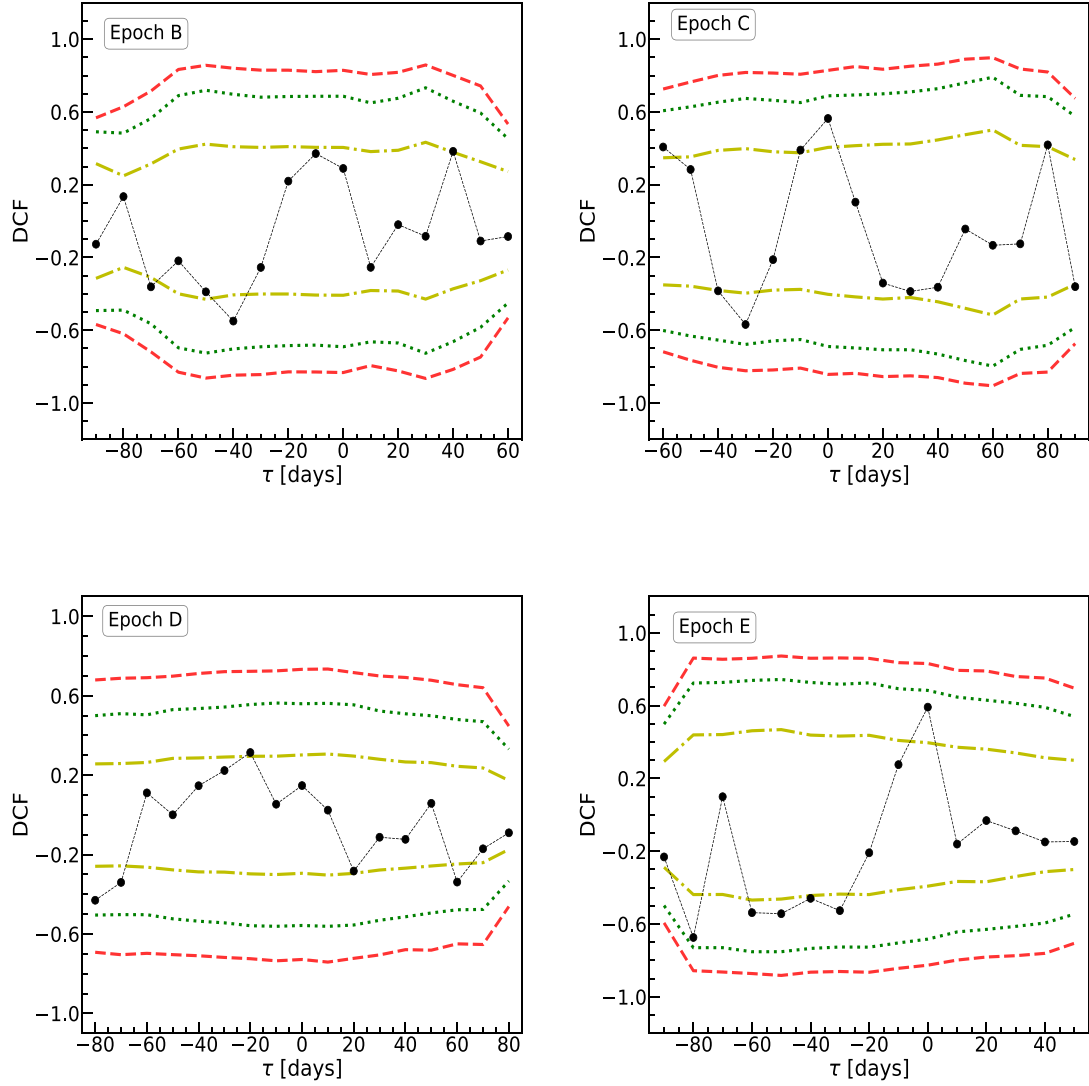


Figure 3. The outcomes of the discrete cross-correlation analysis conducted on the optical V -band and γ -ray light curves during epochs B, C, D, and E. The DCF is indicated by the black dashed line. The significance levels are represented by the yellow dash-dotted line (68.27 per cent, 1σ), green dotted line (95.45 per cent, 2σ), and red dashed line (99.73 per cent, 3σ). A negative lag indicates that the γ -ray flux leads the optical flux variations.

3.1.5 Epoch E (MJD 59905–60005)

The source underwent the major γ -ray flare during this epoch, which is the largest γ -ray flare over the whole time period examined in this work. Such large flux variations were also noticed in the X-ray, UV, and optical bands. The multiwavelength light curve for this epoch is shown in lower right panel of Fig. 2. During this epoch, the γ -ray flux increased about nine times from the average flux level and the optical flux increased nearly eight times compared to the average flux. We conclude that in this epoch the optical and γ -ray flux changes are structurally correlated.

3.2 Cross-correlation analysis

The initial investigation described in Section 3.1 involved visually examining the correlation between changes in optical and γ -ray emissions over different time periods. Furthermore, we explored this correlation in depth by employing advanced cross-correlation analysis methods. Analysing the cross-correlation between variations

in flux across various energy bands allows for the determination of whether emissions in different bands are co-spatial or they emanate from different regions in the jet. In this study, we conduct a cross-correlation analysis using the discrete cross-correlation function (DCF) as outlined in Edelson & Krolik (1988) to measure the time lag between unevenly sampled optical (V -band) light curve and γ -ray light curve binned over 1 d. The significance of the cross-correlation is evaluated through Monte Carlo simulations, with the assumption of a simple PL power spectral density model. This model is defined as $P(\nu) \propto 1/\nu^\beta$, where ν represents the temporal frequency and β denotes the slope. A comprehensive explanation of this methodology is provided by Max-Moerbeck et al. (2014b). We have adopted the value of $\beta_\gamma = 1.5$ (Max-Moerbeck et al. 2014a) and $\beta_{\text{optical}} = 2$ (Goyal 2021). The DCFs between optical and γ -ray light curves for epochs B, C, D, and E are shown in Fig. 3. During these epochs, we detected no significant correlations between variations in optical and γ -ray flux. The results of the DCF analysis are provided in Table 2.

Table 2. The outcomes of the DCF analysis between optical flux and γ -ray flux variations during epochs B, C, D, and E. Here, τ represents the time lag, with negative values indicating that the γ -ray is leading the optical flux variations. The DCF values provide estimates of the cross-correlation coefficient, and the p-value represents the likelihood of observing the correlation under the assumption of the null hypothesis.

Epoch	τ (d)	DCF	p-value
B	-10.0 ± 6.1	0.37	0.365
C	0.0 ± 3.7	0.56	0.139
D	-20.0 ± 14.8	0.31	0.287
E	0.0 ± 3.7	0.59	0.103

3.3 Optical spectral variations

Apart from changes in flux, blazars are also known for exhibiting variations in their spectral characteristics. In general, FSRQs exhibit redder-when-brighter trend (Gu et al. 2006; Bonning et al. 2012; Zhang et al. 2015; Rajput et al. 2019; Safna et al. 2020; Negi et al. 2022). However, bluer-when-brighter pattern is also observed in FSRQ sources (Wu et al. 2011; Rajput et al. 2019, 2020; Safna et al. 2020). The optical and UV spectral regions (V , B , U , $W1$, $M2$, and $W2$ bands) investigated in this paper include contributions from both non-thermal emission from the relativistic jet and thermal emission from the accretion disc. Hence, by examining spectral variations, one can identify the many factors causing the observed flux variations.

To describe the spectral behaviour of the epochs studied in this work, we looked for the variations in the B-V colour against the V-band magnitude. The colour–magnitude diagrams of these epochs are shown in Fig. 4. Due to lack of data, we have not included the colour–magnitude diagram for epoch A. The trend of spectral behaviour during epochs B, C, D, and E was identified by weighted linear least-squares fit, which takes into account errors in both colour and V-band magnitude. We determined the Spearman rank correlation coefficient (R) and probability of obtaining this correlation under the assumption of the null hypothesis (p-value). If $R > 0.5$ or $R < -0.5$ with p-value < 0.05 , the source is considered to have displayed any significant colour trend over the epochs. We found no spectral variations during the epochs considered in this work. The results of the weighted linear least-squares fitting are given in Table 3.

3.4 γ -ray spectral analysis

The inherent distribution of the emitting electrons in blazars may be reflected in the curvature of the γ -ray spectra, which also provides information on the potential acceleration and cooling processes in the jets. The γ -ray spectra of the blazars are fitted by either PL or log parabola (LP) models. The PL model is defined as

$$dN(E)/dE = N_0(E/E_0)^{\Gamma_p}. \quad (1)$$

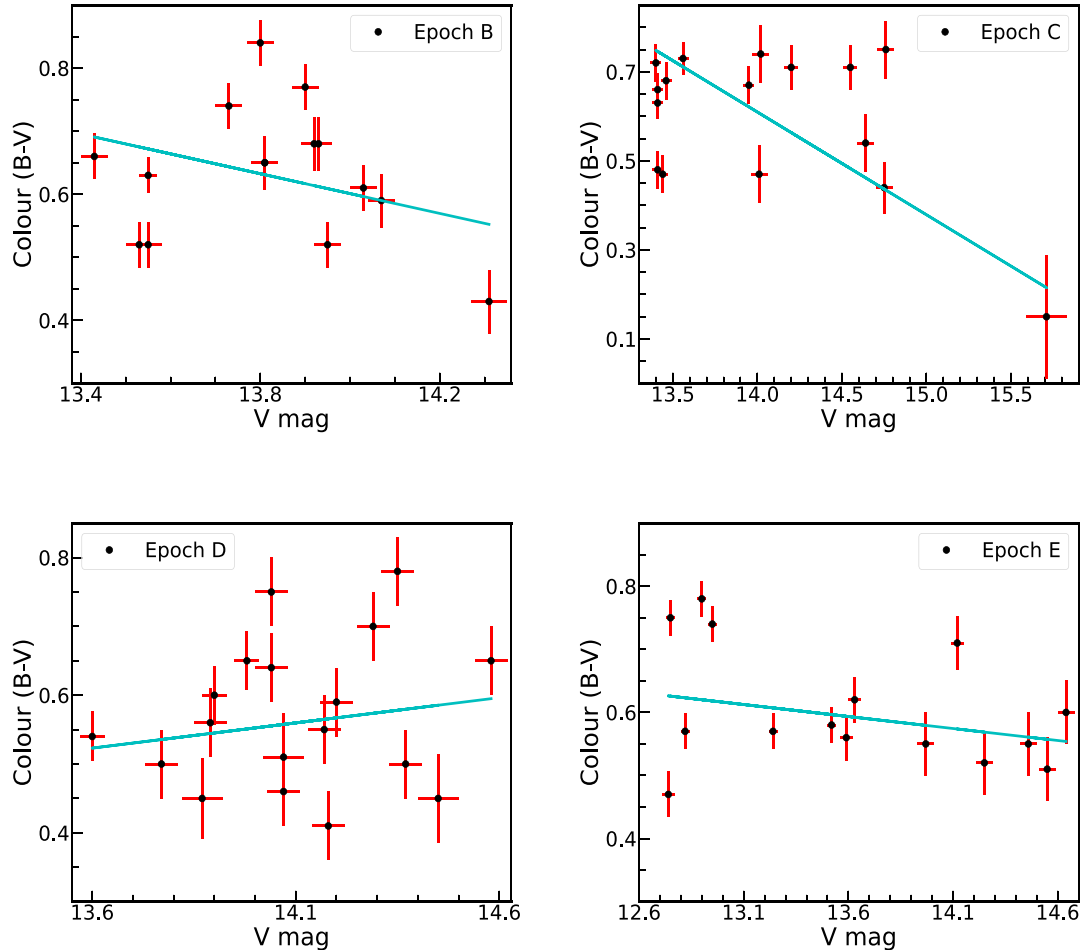


Figure 4. Colour–magnitude diagram for epochs B, C, D, and E. The solid (cyan) line depicts the weighted linear least-squares fit to the data.

Table 3. Results of the weighted linear least-squares fit and Spearman rank correlation test applied to the colour–magnitude diagram during epochs B, C, D, and E. None of the correlations are significant for a chosen significance level of 0.05.

Epoch	Intercept	Slope	R	p-value
B	2.80 ± 1.64	-0.15 ± 0.12	-0.18	0.52
C	3.84 ± 0.63	-0.23 ± 0.04	-0.08	0.76
D	-0.47 ± 1.57	0.07 ± 0.11	0.15	0.56
E	1.11 ± 0.46	-0.04 ± 0.03	-0.28	0.31

Here, $dN(E)/dE$ is the number of photons in $\text{cm}^{-2} \text{s}^{-1} \text{MeV}^{-1}$, N_o is the normalization factor of the energy spectrum, E_o is the scaling factor, and Γ_p is the photon index.

The LP model is defined as

$$dN(E)/dE = N_o(E/E_o)^{-\alpha-\beta \ln(E/E_o)}. \quad (2)$$

Here, α is the photon index at E and β is the curvature index that determines the curvature around the peak.

To evaluate the model that more accurately characterizes the γ -ray spectra (PL against LP), we applied the ML estimation technique outlined in Mattox et al. (1996), utilizing the analysis tool `gtlike`. The `gtlike` tool maximizes the likelihood by employing different optimizers, which determine the optimal spectral parameter values for the best fit. We also calculated the TS_{curve} value, as specified in Nolan et al. (2012), using the following equation:

$$\text{TS}_{\text{curve}} = 2(\log L_{\text{LP}} - \log L_{\text{PL}}). \quad (3)$$

In the above equation, L is the likelihood function. In order to detect significant curvature in the γ -ray spectra, we employed the threshold value $\text{TS}_{\text{curve}} > 16$ (at 4σ level; Mattox et al. 1996). The results of the γ -ray spectral analysis are given in Table 4 and the γ -ray spectra for the selected epochs are shown in Fig. 5. The γ -ray spectra are well fitted with the LP function for all the epochs, except the quiescent epoch A, where the value of TS_{curve} is less than 16.

3.5 Broad-band SED modelling

The source has shown varied flux variability behaviour over the last 15 yr, during which we have detected instances of correlated optical and GeV variations as well as optical flare without γ -ray counterpart. To understand the diverse behaviour of the source during different epochs, we constructed broad-band SEDs and modelled them using one-zone leptonic emission model. To model the broad-band SED, we used the publicly available code JETSET (Tramacere et al. 2009; Tramacere, Massaro & Taylor 2011; Tramacere 2020). JETSET (version 1.2.2) fits numerical models to the data in order to determine the optimal parameter values that best describe the observed data.

Table 4. Spectral analysis results for the γ -ray observations. The γ -ray flux values are expressed in units of $10^{-6} \text{ph cm}^{-2} \text{s}^{-1}$. The PL and LP fits to the γ -ray spectra during these time periods are shown in Fig. 5.

Epoch	Γ_p	PL			α	β	LP			TS_{curve}
		Flux	TS	$-\log L_{\text{PL}}$			Flux	TS	$-\log L_{\text{LP}}$	
A	2.22 ± 0.01	0.04 ± 0.001	117.50	315 166.67	2.16 ± 0.16	0.42 ± 0.78	0.04 ± 0.008	117.82	315 166.50	0.34
B	1.95 ± 0.01	0.92 ± 0.01	19 702.7	385 467.61	1.88 ± 0.002	0.49 ± 0.01	0.88 ± 0.003	19 754.5	385 466.44	42.34
C	2.05 ± 0.02	0.61 ± 0.01	10 498.9	406 121.01	1.96 ± 0.02	0.82 ± 0.13	0.58 ± 0.01	10 552.7	406 094.64	52.74
D	2.04 ± 0.001	0.49 ± 0.001	8837.58	415 533.94	1.97 ± 0.02	0.56 ± 0.12	0.47 ± 0.01	8862.74	415 521.70	24.48
E	2.05 ± 0.001	1.27 ± 0.007	23 812.1	378 575.73	1.97 ± 0.02	0.83 ± 0.09	1.20 ± 0.02	23 812.4	378 520.98	109.50

The photometric observations taken in both UV and optical wavelengths during each epoch were averaged filterwise to generate a single photometric data point for each epoch. On the other hand, the average spectra for X-rays and γ -rays were created using all of the data that were available for the 100-d span in each of the epochs. Since the EC process primarily accounts for the high-energy γ -ray emission in the FSRQs (Paliya, Sahayanathan & Stalin 2015; Shah et al. 2017; Rajput et al. 2019, 2020), we used synchrotron, SSC, and EC processes to model our SEDs. In the one-zone leptonic emission model, the spherical blob of radius R is located at a distance of R_{H} from the central black hole. It is postulated that this spherical region is injected with non-thermally accelerated electrons that follow a distribution characterized by a broken PL. The broken PL distribution of electrons is defined as follows:

$$N(\gamma)d\gamma = \begin{cases} K\gamma^{-p}d\gamma, & \gamma_{\text{min}} < \gamma < \gamma_{\text{break}}, \\ K\gamma_{\text{break}}^{p_1-p}\gamma^{-p_1}d\gamma, & \gamma_{\text{break}} < \gamma < \gamma_{\text{max}}, \end{cases} \quad (4)$$

where γ is the electron Lorentz factor, N is the electron density in units of cm^{-3} , and K is the normalization constant. p and p_1 are the low- and high-energy spectral slopes, and γ_{min} , γ_{max} , and γ_{break} are the Lorentz factors corresponding to the low-energy cut-off, high-energy cut-off, and turn over energy, respectively. The emission region (spherical blob), which is moving down the jet with the bulk Lorentz factor Γ , is permeated with the magnetic field B . The relativistic electrons interact with the magnetic field and produce synchrotron radiation. The SSC emission is produced by the same synchrotron photons generated within the jet (Tramacere et al. 2009). The seed photons for the EC process are external to the jet, which are produced (1) from the accretion disc (Dermer & Schlickeiser 2002; Ghisellini, Tavecchio & Ghirlanda 2009), (2) from BLR (Dermer et al. 2009), and (3) from dust torus (Sikora et al. 2008). The external photons that directly come from the accretion disc and participate in the EC process have luminosity L_{disc} and temperature T_{disc} . The reprocessed UV photons from the BLR, which is located at a distance of R_{BLR} from the black hole, and IR photons from the dust torus, which is located at a distance of R_{DT} with a temperature of T_{DT} , are involved in the EC process. The fractions of L_{disc} reprocessed by the BLR and dust torus are given as τ_{BLR} and τ_{DT} , respectively.

We have determined the size of the emission region R , which is defined as $R \leq cT_{\text{min}}\delta/(1+z)$, where T_{min} is the minimum variability time-scale and δ denotes the Doppler factor. We have calculated the minimum variability time-scale for the γ -ray light curve using the methodology that models flares with an exponential profile, as outlined in Burbidge, Jones & O’Dell (1974):

$$T_{\text{min}} = \Delta t / \ln(F_2/F_1). \quad (5)$$

Here, $\Delta t = |t_2 - t_1|$ and F_2 and F_1 are the flux values at times t_2 and t_1 , respectively. The minimum variability time-scale is calculated to be ~ 7.23 h. We have adopted the Doppler factor value for the source as $\delta = 18.2$, which has been determined using the one-zone

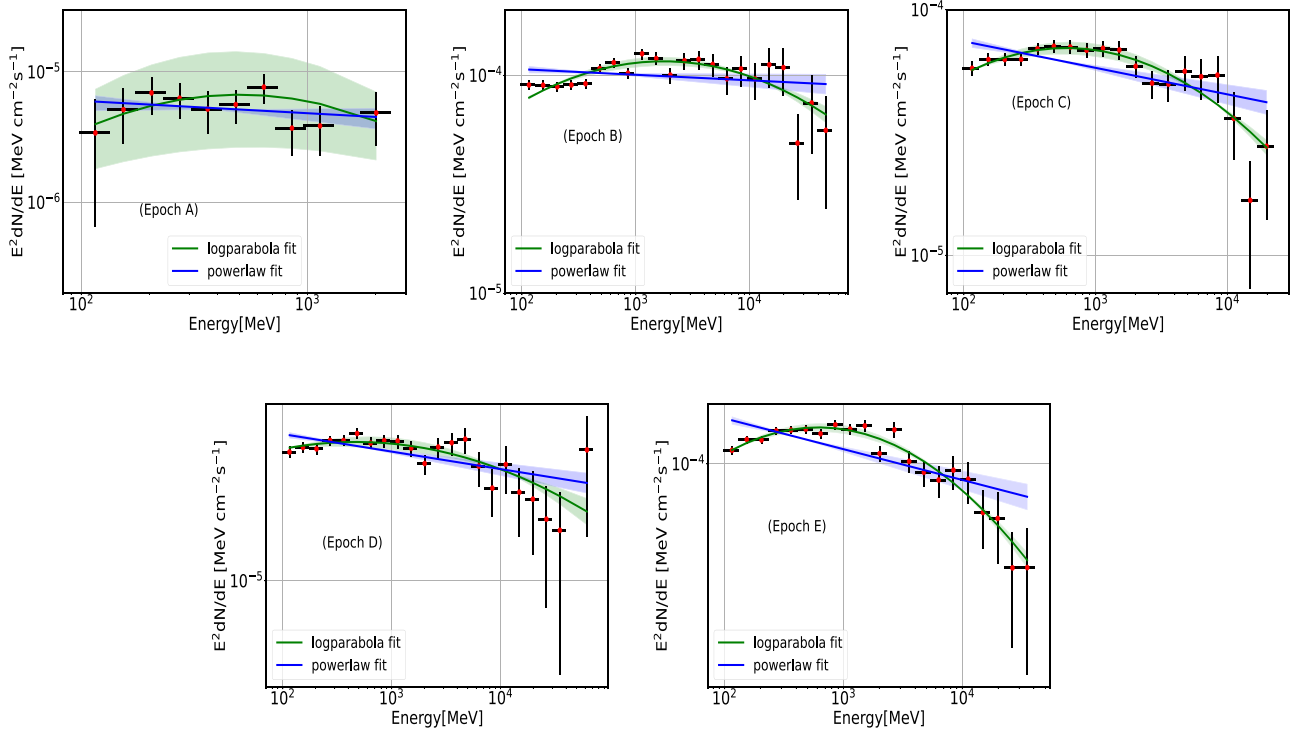


Figure 5. PL and LP fits to the γ -ray spectra for epochs A, B, C, D, and E with 1σ uncertainty. Among these, the PL fit provides a better description of the γ -ray spectra in epoch A, while the LP fit better explains the γ -ray spectra in epochs B, C, D, and E. Refer to Table 4 for detailed results.

leptonic emission model by Paliya et al. (2017). Using the values of T_{\min} and δ , we have approximated the size of emission region to be $8.24 \times 10^{15} \text{ cm} \sim 8 \times 10^{15} \text{ cm}$. Furthermore, assuming that this blob covers the whole cross-section of the jets, we have estimated the distance of this blob from the central black hole using the relation $R_{\text{H}} = R/\phi$, where ϕ represents the opening angle. The intrinsic opening angle for Ton 599 is estimated as 0.58° ($\sim 0.01 \text{ rad}$) based on observations conducted with the 15.4-GHz Very Long Baseline Array (VLBA) from the 2-cm VLBA MOJAVE (Monitoring Of Jets in Active galactic nuclei with VLBA Experiments) programme (Pushkarev et al. 2009). Utilizing the values of R and ϕ , we estimate that the location of the emission region is located at roughly $8 \times 10^{17} \text{ cm}$ away from the central black hole.

We have considered a value for L_{disc} equal to $4.5 \times 10^{45} \text{ erg s}^{-1}$, which was determined through the application of a one-zone leptonic emission model in studies by Ghisellini et al. (2010) and Paliya et al. (2017). The inner radius of the spherical shell like BLR ($R_{\text{BLR}_{\text{in}}}$) is considered to be $0.01 \text{ pc} \sim 3.1 \times 10^{16} \text{ cm}$ (Donea & Protheroe 2003). The outer radius of the BLR ($R_{\text{BLR}_{\text{out}}}$) is estimated to be around $2.1 \times 10^{17} \text{ cm}$ using the relationship $R_{\text{BLR}} = 10^{17} L_{\text{disc}, 45}^{1/2}$ cm, where $L_{\text{disc}, 45}$ represents the luminosity of the accretion disc in units of $10^{45} \text{ erg s}^{-1}$. This estimation is based on the assumption that the BLR radius scales in relation to the square root of the luminosity of the accretion disc (Ghisellini & Tavecchio 2008). Moreover, it is posited that the spherical shell like torus is situated at a distance $R_{\text{DT}} = 2.5 \times 10^{18} L_{\text{disc}, 45}^{1/2} \text{ cm}$ (Ghisellini & Tavecchio 2008), which is approximately equivalent to $5 \times 10^{18} \text{ cm}$. We have assumed that the fraction of the L_{disc} reprocessed by the BLR (τ_{BLR}) is 0.1 and by the dust torus (τ_{DT}) is 0.5 (Ghisellini et al. 2010). Furthermore, the disc temperature T_{disc} and dust torus temperature T_{DT} are assumed to be at their typical values of $1.0 \times 10^5 \text{ K}$ (Patel & Chitnis 2020) and $1.0 \times 10^3 \text{ K}$ (Donea & Protheroe 2003), respectively, in our study.

Table 5. Values of the frozen parameters for the one-zone leptonic model fits to the observed SEDs during the five epochs.

Name of the parameters	Values
γ_{\min}	40
γ_{break}	1.1×10^3
γ_{\max}	1.0×10^4
T_{DT}	1000 K
R_{DT}	$5 \times 10^{18} \text{ cm}$
τ_{DT}	0.5
τ_{BLR}	0.1
$R_{\text{BLR}_{\text{in}}}$	$3.1 \times 10^{16} \text{ cm}$
$R_{\text{BLR}_{\text{out}}}$	$2.1 \times 10^{17} \text{ cm}$
L_{disc}	$4.5 \times 10^{45} \text{ erg s}^{-1}$
T_{disc}	$1.0 \times 10^5 \text{ K}$
R	$8.0 \times 10^{15} \text{ cm}$
R_{H}	$8.0 \times 10^{17} \text{ cm}$
Cold proton to relativistic electron ratio	0.1

The ratio of cold protons to relativistic electrons is taken as 0.1 in our SED analysis (Ghisellini 2012).

In one-zone leptonic model, the characteristics of the observed SED are primarily determined by 19 parameters. Five parameters, namely p , p_1 , N , B , and Γ , are chosen to be free, while the remaining 14 parameters are chosen to be frozen. The purpose of parameter freezing is to compare the changes in certain parameters, such as the magnetic field, bulk Lorentz factor, particle density, etc., between quiescent and flaring epochs. Details of frozen parameters are given in Table 5. In order to investigate the distinct correlation behaviour between optical and γ -ray flux variations during different flaring epochs, we initially fitted the quiescent epoch to acquire the values for the parameters γ_{\min} , γ_{\max} , and γ_{break} . The fitting process using the same frozen parameters and the previously acquired values of

Table 6. Results of the broad-band SED fitting during the epochs A, B, C, D, and E.

Parameters	Epoch A	Epoch B	Epoch C	Epoch D	Epoch E
p	2.29 ± 0.31	2.40 ± 0.11	2.04 ± 0.06	2.55 ± 0.11	2.17 ± 0.13
p_1	4.03 ± 0.37	3.20 ± 0.15	3.18 ± 0.08	3.60 ± 0.19	3.85 ± 0.21
$N (\times 10^3 \text{ cm}^{-3})$	0.98 ± 0.20	1.19 ± 0.15	1.31 ± 0.09	0.89 ± 0.11	0.84 ± 0.11
B (G)	1.63 ± 0.29	1.51 ± 0.10	1.51 ± 0.07	2.05 ± 0.15	1.73 ± 0.14
Bulk Lorentz factor	22.48 ± 2.78	37.31 ± 1.75	28.64 ± 0.83	37.37 ± 1.87	38.54 ± 2.01

γ_{\min} , γ_{\max} , and γ_{break} from the fitting during the quiescent epoch was repeated for the other epochs B, C, D, and E with the selection of free parameters. Our SED analysis shows that the leptonic scenario provides a good fit to the observed broad-band SED across all the epochs. The resultant best-fitting parameters for the selected epochs are given in Table 6 and the fitted SEDs are shown in Fig. 6.

4 DISCUSSION

4.1 Connection between optical and γ -ray flux variations

Over a span of around 15 yr of study, Ton 599 has shown varied correlated behaviour between optical V-band flux and γ -ray flux variations. We found two cases, where (1) both the optical flux and the γ -ray flux showed flaring behaviour and (2) an increase in optical flux without a corresponding increase in γ -ray flux is observed. We chose five epochs A, B, C, D, and E based on the distinct behaviour between optical V-band and γ -ray flux variations. During epoch A, the source was in its quiescent state in each waveband. During epochs B, C, and E, there was a structural correlation between the variations in optical and γ -ray flux. However, during epoch D, the source exhibited an optical flare without a corresponding γ -ray response. Our investigation involving linear regression analysis on the logarithmic values of γ -ray flux and optical flux suggests a similar trend. The linear least-squares fits are shown in Fig. 7, depicting the logarithm of γ -ray flux plotted against the logarithm of optical flux. The outcomes of the linear regression analysis are given in Table 7. Moreover, we employed the sophisticated DCF to cross-correlate the optical V-band and γ -ray light curves, aiming to establish whether there is a correlation between variations in the optical flux and γ -ray flux. We found that there are weakly significant correlations between the optical and γ -ray flux variations. Given the observed structural similarities between these two energy bands, this low significance may result from the relatively low amount of optical data used.

A time lag of a few days within the period of 2017 October–December, falling within the time frame of epoch B considered here, was previously identified by Prince (2019). In the cross-correlation study of bright blazars, Liodakis et al. (2018, 2019) found that the time lag between optical and γ -ray bands is generally small. Moreover, de Jaeger et al. (2023) found that the time lag distribution between optical and γ -ray bands is consistent with zero lags. These results indicate that the optical and γ -ray flux emission regions are co-spatial and favour leptonic emission model of blazars, where the same relativistic electron population is accountable for both the optical and γ -ray emission. Given the scenario that both optical and γ -ray emissions are proportionate to the number of emitting electrons, it is plausible that variations in the electron population of the jet lead to the correlation between these two types of flux variations, as proposed by D’Ammando et al. (2011).

4.2 γ -ray spectra

The γ -ray spectral shape of blazars can yield valuable information about the inherent characteristics of the jets such as the distribution of emitting particles. In particular, these γ -ray spectra can help us determine whether there is any absorption of γ -rays within the emission region and can also reveal whether γ -ray emissions are attributed to a single component of the jet or multiple components. The high-energy γ -ray spectra of FSRQ sources are better explained by the broken PL or LP model (Abdo et al. 2010a; Paliya et al. 2015; Rajput et al. 2019, 2020; Sahakyan 2020; Rajput & Pandey 2021). The curvature observed in the γ -ray spectra of FSRQs may be attributed to external factors, such as the absorption of γ -rays through photon–photon pair production within the BLR (Poutanen & Stern 2010), and the impact of the Klein–Nishina effect on the IC scattering of BLR photons by relativistic jet electrons with a curved distribution (Cerruti et al. 2013). However, both the effects account for the IC scattering of the BLR photons, whereas in the large number of FSRQs the γ -ray emission site lies outside the BLR and γ -ray emission is not produced by the IC scattering of the BLR photons (Costamante et al. 2018). Our SED analysis also indicates that the γ -ray emission is produced by the IC scattering of the IR photons from the dusty torus.

In our work, the LP model fits the γ -ray spectra in the flaring epochs (and orphan optical flare epoch) adequately, whereas the PL model fits the γ -ray spectra in the quiescent epoch well. The curvature observed in the γ -ray spectra is probably caused by the inherent characteristics of the electron distribution that produces emission. These electrons follow either a cut-off energy distribution or an LP energy distribution. However, during quiescent epoch the low quality of photons data available for analysis makes it challenging for us to identify this curvature. In the LP model fits to γ -ray spectra, the parameters α and β convey crucial information about the properties of the γ -ray spectra. Changes in the α and β values are reflected in the shape of γ -ray spectra. We looked for the variations in the α and β parameters against γ -ray flux during epochs B, C, D, and E, which are shown in Fig. 8. We conducted an analysis to find a correlation between the α and β parameters and the γ -ray flux, employing the Spearman rank test. We considered that the correlation is significant if the Spearman rank correlation coefficient >0.5 or <-0.5 , along with a p-value < 0.05 . We observed that the parameter α showed no significant pattern, and the curvature parameter β exhibited a mild negative correlation with γ -ray flux throughout all epochs. The results of Spearman rank test are given in Table 8. Decreasing trend of β with increasing flux was also noticed in the study of 3LAC (the third catalogue of AGNs detected by the *Fermi*) sources by Ackermann et al. (2015). According to Coogan, Brown & Chadwick (2016), the variations in the location of the γ -ray emission area during various activity levels of the sources may be responsible for these distinct spectral behaviours of the γ -ray spectra. Such varied spectral behaviour could also be caused by a change in

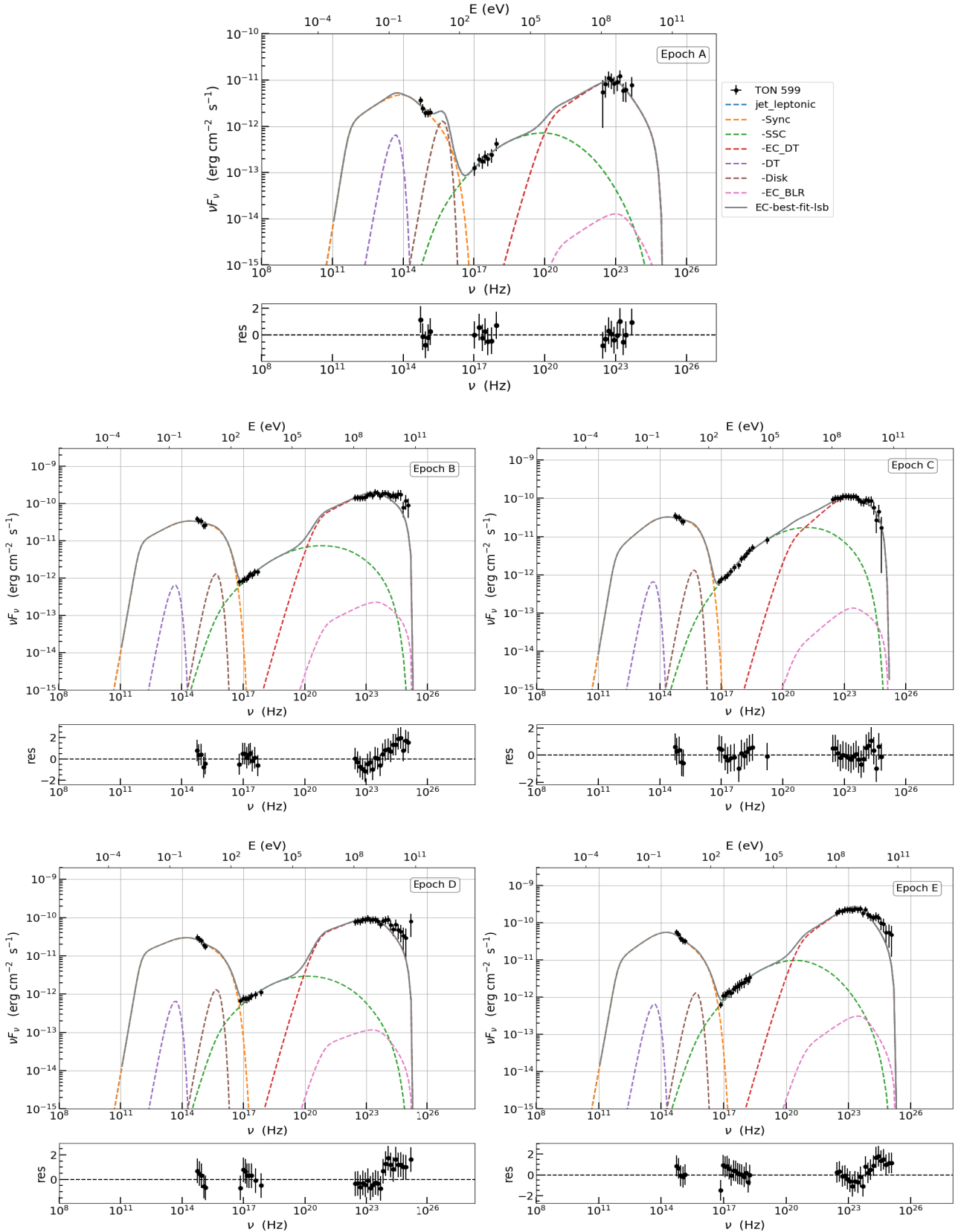


Figure 6. Observed broad-band SED along with the one-zone leptonic emission model fit during epochs A, B, C, D, and E (top panel) and the residuals (bottom panel). Here, the solid line is the best fit to the SED, orange dashed line represents the emission from synchrotron process, green dashed line represents the emission from SSC process, red dashed line represents the EC emission from dusty torus, and pink dashed line represents the EC emission from BLR. Purple and brown dashed lines represent the thermal emissions from the dusty torus and accretion disc, respectively. The fit to the quiescent state is applied for determining the values of the parameters γ_{\min} , γ_{\max} , and γ_{break} in the subsequent epochs modelled in this study.

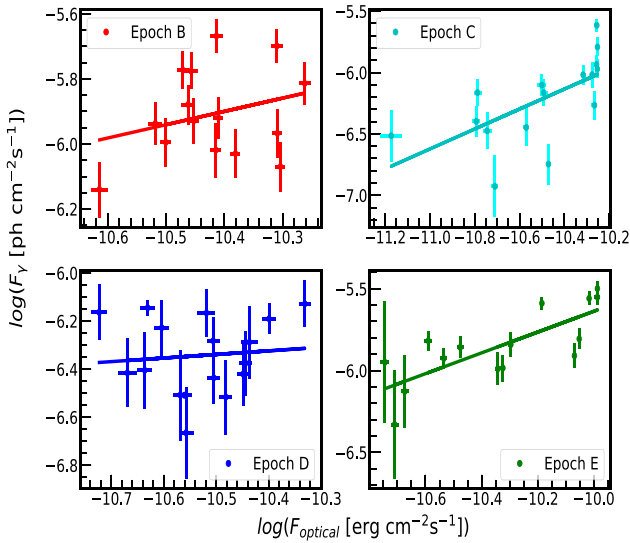


Figure 7. γ -ray versus optical V-band fluxes during epochs B, C, D, and E.

Table 7. The results obtained by applying linear regression on the logarithm of γ -ray flux and optical flux during epochs B, C, D, and E.

Epoch	Intercept	Slope	Correlation coefficient	p-value
B	-1.65 ± 4.05	0.41 ± 0.39	0.28	0.31
C	2.31 ± 2.76	0.81 ± 0.26	0.64	0.008
D	-4.77 ± 4.17	0.15 ± 0.40	0.10	0.71
E	0.71 ± 1.53	0.64 ± 0.15	0.77	0.001

the IC peak frequency, where the external photon field is responsible for producing the γ -ray emission in FSRQs (Rajput et al. 2020).

4.3 Broad-band spectral energy distribution

In our study, we found instances of both optical and γ -ray flares as well as optical flare without its corresponding γ -ray counterpart. Lioudakis et al. (2019) investigated for a correlation between optical and GeV flux changes in 178 blazars and found that in nearly 50 percent of the blazars, optical flares occurred without their γ -ray counterparts. A few blazars with complex behaviour between changes in optical and γ -ray flux were also studied by Chatterjee et al. (2013), Cohen et al. (2014), and Rajput et al. (2019, 2020). Hadronic processes could provide a possible explanation for optical flux variations without γ -ray counterparts or vice versa (Mücke & Protheroe 2001). Furthermore, the leptonic scenario of blazars favours a close correlation between changes in the optical and GeV flux. However, results from Rajput et al. (2019, 2020) indicate that different correlation behaviour between optical and γ -ray flux changes are well explained by one-zone leptonic model scenario.

In this work, we performed broad-band SED modelling using a one-zone leptonic emission model to model the five epochs considered here. The leptonic model provides a good fit during all the epochs with the seed photons for the EC process from the torus. The source was in a quiescent condition during epoch A, therefore we first fitted the broad-band SED for epoch A and then looked for changes in parameters in other epochs relative to the quiescent epoch. The accretion disc component is clearly evident in the broad-band SED during the quiescent phase, but synchrotron radiation

dominates the optical–UV emission during epochs B, C, D, and E. The source showed both optical and γ -ray flares during epochs B, C, and E. During epochs B and E, the bulk Lorentz factor was roughly 1.5 times higher than the quiescent epoch A. Furthermore, there was an increase in electron density and a decrease in the magnetic field during period B. In contrast, during period E, there was a decrease in electron density and an increase in the magnetic field. The enhanced optical and γ -ray fluxes in these two time intervals may be attributed to the increased bulk Lorentz factor and changes in electron density and magnetic field. In comparison to the quiescent period, the bulk Lorentz factor changed slightly during epoch C, and there was also decrease in the magnetic field. However, the electron density increased during epoch C, which might be accountable for the optical and γ -ray flares during this epoch.

During epoch D, when the source showed an orphan optical flare, the bulk Lorentz factor increased almost 1.5 times, while the electron density decreased when compared to epoch A. Additionally, the magnetic field was at its peak during this epoch. Consequently, the orphan optical flare can be the result of the increased magnetic field and bulk Lorentz factor during epoch D. According to Marscher & Gear (1985), the change in magnetic field can affect the synchrotron emission in the jet; however, the γ -ray emission will be unperturbed by the change in the magnetic field. The presence of increased optical polarization measurements and X-ray flare can support this argument. A significant X-ray flare is observed during this time (see Fig. 1), which is dominated by SSC process (the same photons emitted by the synchrotron process are involved in the EC process); however, the optical polarization measurements are not available at this time. From SED analysis, we draw the conclusion that the leptonic model explains the optical–GeV variations during the various epochs in Ton 599.

5 SUMMARY

We investigated the correlation between the changes in optical V-band and GeV flux in the FSRQ Ton 599 for the time period MJD 54686–60008. Our study includes (1) the identification of the epochs exhibiting optical or γ -ray flare, (2) cross-correlation analysis between optical flux and γ -ray flux variations, (3) analysis of optical spectral variations, (4) analysis of γ -ray spectra, and (5) broad-band SED modelling with a one-zone leptonic emission model for the chosen epochs. We summarize the results below.

- (i) In the period of around 15 yr, we selected five epochs A, B, C, D, and E. The source was in its quiescent state during epoch A. Our visual inspections indicated that in epochs B, C, and E, the source showed variations in both optical and γ -ray emissions, showing structural similarities. However, during epoch D, the source showed an optical flare, without a clear γ -ray counterpart. The source was in its highest flaring state during epoch E.
- (ii) Through cross-correlation analysis, we identified a weak linear correlation between optical and γ -ray light curves.
- (iii) We found no optical spectral variations during the epochs.
- (iv) During the quiescent period, the γ -ray spectra of the source were well described by the PL model, while during the flaring periods, the γ -ray spectra were best described by the LP model.
- (v) During all the epochs, from SED modelling, we found the γ -ray emission to be produced by EC process, where the source of seed photons is the torus. Our SED analysis showed that during the quiescent period, the optical–UV emission was caused by the accretion disc component, but during the flaring periods, the synchrotron emission was the cause for the optical–UV emission.

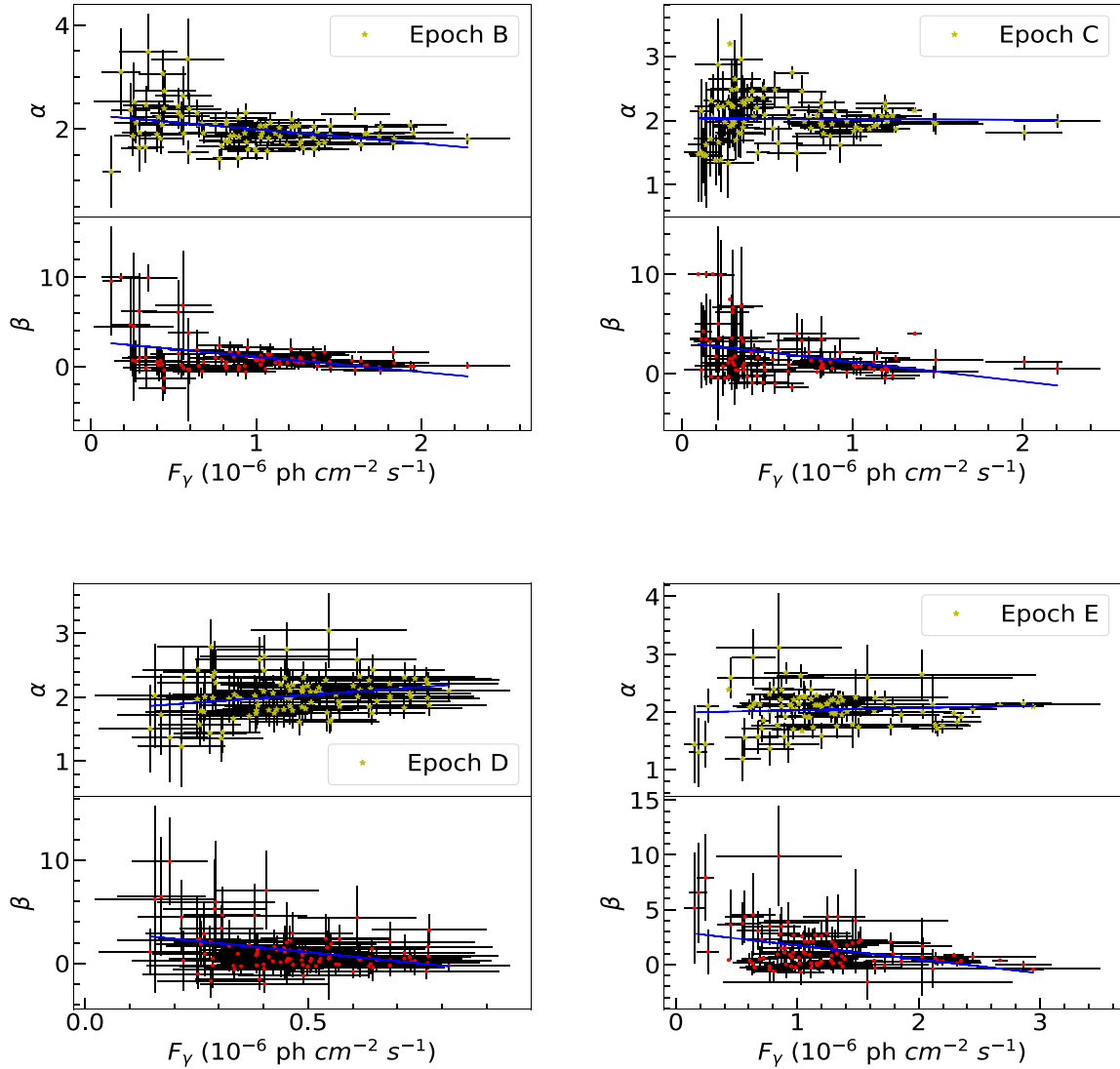


Figure 8. Correlation between the parameters α and β and the γ -ray flux. The solid (blue) line represents the least-squares fit applied to the data.

Table 8. Results of the Spearman rank test for the correlation of α and β parameters with γ -ray flux. The plots of α and β parameters versus γ -ray flux are shown in Fig. 8.

Epoch	α		β	
	R	p-value	R	p-value
B	-0.33	0.002	-0.21	0.04
C	0.06	0.58	-0.34	0.001
D	0.26	0.01	-0.27	0.007
E	0.02	0.84	-0.30	0.003

The varied behaviour observed in our work between the changes in optical and GeV flux could be explained by changes in the magnetic field, the bulk Lorentz factor, and the electron density.

ACKNOWLEDGEMENTS

We are thankful to the anonymous referee for providing valuable feedback, which helped to improve the manuscript. BR gratefully

acknowledges support by ANID BASAL project FB210003 and FONDECYT Postdoctorado 3230631. WM-M gratefully acknowledges support by the ANID BASAL project FB210003. Part of this work was supported by the Polish funding agency National Science Centre, project 2017/26/A/ST9/00756 (MAESTRO 9). This research has made use of data from *Fermi* Science Support Center, which were made available by NASA's Goddard Space Flight Center (GSFC). The HEASARC, a service of GSFC, is used to obtain the data, software, and online tools. This study used *NuSTAR* data as well as NUSTARDAS, which was collaboratively developed by the California Institute of Technology (Caltech, USA) and the ASI Science Data Center (ASDC, Italy). We are thankful for photometry program from Paul Smith's monitoring program at the SO, which is supported by *Fermi* Guest Investigator grants NNX08AW56G, NNX09AU10G, NNX12AO93G, and NNX15AU81G. This study utilized ASAS-SN data, which was partially funded by the Alfred P. Sloan Foundation grant G-2021-14192 and Gordon and Betty Moore Foundation grants GBMF5490 and GBMF10501 to the Ohio State University. This research utilized

the publicly accessible numerical code JETSET,⁸ developed by A. Tramacere.

DATA AVAILABILITY

The multiwavelength data utilized in this study are publicly accessible from the *Fermi*-LAT,⁹ *Swift*-XRT,¹⁰ *NuSTAR*,¹¹ *Swift*-UVOT,¹² SO,¹³ and ASAS-SN.¹⁴

REFERENCES

- Abdo A. A. et al., 2010a, *ApJ*, 710, 1271
 Abdo A. A. et al., 2010b, *ApJ*, 715, 429
 Abdo A. A. et al., 2010c, *ApJ*, 716, 30
 Abdollahi S. et al., 2020, *ApJS*, 247, 33
 Abdollahi S. et al., 2022, *ApJS*, 260, 53
 Ackermann M. et al., 2015, *ApJ*, 810, 14
 Acosta Pulido J. A., Redondo J., Carnerero M. I., Raiteri C. M., Villata M., Larionov V. M., Kopatskaya E. N., *GASP-WEBT Collaboration*, 2017, *Astron. Telegram*, 10949, 1
 Aharonian F. A., 2000, *New Astron.*, 5, 377
 Antonucci R., 1993, *ARA&A*, 31, 473
 Arnaud K. A., 1996, in Jacoby G. H., Barnes J., eds, *ASP Conf. Ser. Vol. 101, Astronomical Data Analysis Software and Systems V*. *Astron. Soc. Pac.*, San Francisco, p. 17
 Atwood W. B. et al., 2009, *ApJ*, 697, 1071
 Bhatta G. et al., 2023, *MNRAS*, 520, 2633
 Blandford R. D., Rees M. J., 1978, in Wolfe A. M., ed., *Pittsburgh Conference on BL Lac Objects*. University of Pittsburgh Press, Pittsburgh, PA, A79-30026, p. 328
 Blazewski M., Sikora M., Moderski R., Madejski G. M., 2000, *ApJ*, 545, 107
 Boettcher M., Mause H., Schlickeiser R., 1997, *A&A*, 324, 395
 Bonning E. W. et al., 2009, *ApJ*, 697, L81
 Bonning E. et al., 2012, *ApJ*, 756, 13
 Böttcher M., 2007, *Ap&SS*, 309, 95
 Böttcher M., Reimer A., Sweeney K., Prakash A., 2013, *ApJ*, 768, 54
 Breeveld A. A., Landsman W., Holland S. T., Roming P., Kuin N. P. M., Page M. J., 2011, in McEnery J. E., Racusin J. L., Gehrels N., eds, *AIP Conf. Proc. Vol. 1358, Gamma Ray Bursts 2010*. *Am. Inst. Phys.*, New York, p. 373
 Burbidge G. R., Jones T. W., O’Dell S. L., 1974, *ApJ*, 193, 43
 Burrows D. N. et al., 2005, *Space Sci. Rev.*, 120, 165
 Carrasco L., Escobedo G., Recillas E., Porras A., Chavushyan V., Mayya D. Y., 2017, *Astron. Telegram*, 10932, 1
 Cerruti M., Dermer C. D., Lott B., Boisson C., Zech A., 2013, *ApJ*, 771, L4
 Cerruti M., Zech A., Boisson C., Emery G., Inoue S., Lenain J. P., 2019, *MNRAS*, 483, L12
 Chatterjee R. et al., 2012, *ApJ*, 749, 191
 Chatterjee R. et al., 2013, *ApJ*, 763, L11
 Cheung C. C., Gasparini D., Buson S., 2017, *Astron. Telegram*, 10931, 1
 Cohen D. P., Romani R. W., Filippenko A. V., Cenko S. B., Lott B., Zheng W., Li W., 2014, *ApJ*, 797, 137
 Coogan R. T., Brown A. M., Chadwick P. M., 2016, *MNRAS*, 458, 354
 Costamante L., Cutini S., Tosti G., Antonini E., Tramacere A., 2018, *MNRAS*, 477, 4749
 D’Ammando F. et al., 2011, *A&A*, 529, A145
 de Jaeger T. et al., 2023, *MNRAS*, 519, 6349
 Dermer C. D., Schlickeiser R., 2002, *ApJ*, 575, 667
 Dermer C. D., Finke J. D., Krug H., Böttcher M., 2009, *ApJ*, 692, 32
 Dickey J. M., Lockman F. J., 1990, *ARA&A*, 28, 215
 Diltz C., Böttcher M., 2016, *ApJ*, 826, 54
 Donea A.-C., Protheroe R. J., 2003, *Astropart. Phys.*, 18, 377
 Dutka M. S. et al., 2013, *ApJ*, 779, 174
 Edelson R. A., Krolik J. H., 1988, *ApJ*, 333, 646
 Fan J. H. et al., 2006, *PASJ*, 58, 797
 Foffano L., Prandini E., Franceschini A., Paiano S., 2019, *MNRAS*, 486, 1741
 Fossati G., Maraschi L., Celotti A., Comastri A., Ghisellini G., 1998, *MNRAS*, 299, 433
 Garrappa S., Valverd J., 2023, *Astron. Telegram*, 15859, 1
 Gehrels N. et al., 2004, *ApJ*, 611, 1005
 Ghisellini G., 2012, *MNRAS*, 424, L26
 Ghisellini G., Madau P., 1996, *MNRAS*, 280, 67
 Ghisellini G., Maraschi L., 1989, *ApJ*, 340, 181
 Ghisellini G., Tavecchio F., 2008, *MNRAS*, 387, 1669
 Ghisellini G., Tavecchio F., Ghirlanda G., 2009, *MNRAS*, 399, 2041
 Ghisellini G., Tavecchio F., Foschini L., Ghirlanda G., Maraschi L., Celotti A., 2010, *MNRAS*, 402, 497
 Ghisellini G., Tavecchio F., Foschini L., Ghirlanda G., 2011, *MNRAS*, 414, 2674
 Goyal A., 2021, *ApJ*, 909, 39
 Gu M. F., Lee C. U., Pak S., Yim H. S., Fletcher A. B., 2006, *A&A*, 450, 39
 Harrison F. A. et al., 2013, *ApJ*, 770, 103
 Hewett P. C., Wild V., 2010, *MNRAS*, 405, 2302
 Impey C. D., Neugebauer G., 1988, *AJ*, 95, 307
 Kalberla P. M. W., Burton W. B., Hartmann D., Arnal E. M., Bajaja E., Morras R., Pöppel W. G. L., 2005, *A&A*, 440, 775
 Kochanek C. S. et al., 2017, *PASP*, 129, 104502
 Konigl A., 1981, *ApJ*, 243, 700
 Liao N. H., Bai J. M., Liu H. T., Weng S. S., Chen L., Li F., 2014, *ApJ*, 783, 83
 Liodakis I., Romani R. W., Filippenko A. V., Kiehlmann S., Max-Moerbeck W., Readhead A. C. S., Zheng W., 2018, *MNRAS*, 480, 5517
 Liodakis I., Romani R. W., Filippenko A. V., Kocevski D., Zheng W., 2019, *ApJ*, 880, 32
 MacDonald N. R., Marscher A. P., Jorstad S. G., Joshi M., 2015, *ApJ*, 804, 111
 Mannheim K., 1993, *A&A*, 269, 67
 Mao P., Urry C. M., Massaro F., Paggi A., Cauteruccio J., Künzel S. R., 2016, *ApJS*, 224, 26
 Marscher A. P., Gear W. K., 1985, *ApJ*, 298, 114
 Mattox J. R. et al., 1996, *ApJ*, 461, 396
 Max-Moerbeck W. et al., 2014a, *MNRAS*, 445, 428
 Max-Moerbeck W., Richards J. L., Hovatta T., Pavlidou V., Pearson T. J., Readhead A. C. S., 2014b, *MNRAS*, 445, 437
 Mücke A., Protheroe R. J., 2001, *Astropart. Phys.*, 15, 121
 Mücke A., Protheroe R. J., Engel R., Rachen J. P., Stanev T., 2003, *Astropart. Phys.*, 18, 593
 Mukherjee R., *VERITAS Collaboration*, 2017, *Astron. Telegram*, 11075, 1
 Negi V., Joshi R., Chand K., Chand H., Wiita P., Ho L. C., Singh R. S., 2022, *MNRAS*, 510, 1791
 Nolan P. L. et al., 2012, *ApJS*, 199, 31
 Padovani P., Giommi P., 1995, *ApJ*, 444, 567
 Paliya V. S., Sahayanathan S., Stalin C. S., 2015, *ApJ*, 803, 15
 Paliya V. S., Diltz C., Böttcher M., Stalin C. S., Buckley D., 2016, *ApJ*, 817, 61
 Paliya V. S., Marcotulli L., Ajello M., Joshi M., Sahayanathan S., Rao A. R., Hartmann D., 2017, *ApJ*, 851, 33
 Patel S. R., Chitnis V. R., 2020, *MNRAS*, 492, 72
 Patel S. R., Chitnis V. R., Shukla A., Rao A. R., Nagare B. J., 2018, *ApJ*, 866, 102
 Poutanen J., Stern B., 2010, *ApJ*, 717, L118
 Prince R., 2019, *ApJ*, 871, 101
 Prince R., 2023, *Astron. Telegram*, 15854, 1

⁸<https://github.com/andreatramacere/jetset>

⁹<https://fermi.gsfc.nasa.gov/ssc/data/access/lat/>

¹⁰<https://heasarc.gsfc.nasa.gov/docs/archive.html>

¹¹<http://heasarc.gsfc.nasa.gov/docs/nustar/analysis/>

¹²<https://www.ssdc.asi.it/cgi-bin/swiftuvarchint>

¹³<http://james.as.arizona.edu/~psmith/Fermi/>

¹⁴<https://asas-sn.osu.edu/>

- Pushkarev A. B., Kovalev Y. Y., Lister M. L., Savolainen T., 2009, *A&A*, 507, L33
- Rajput B., Pandey A., 2021, *Galaxies*, 9, 118
- Rajput B., Stalin C. S., Sahayanathan S., Rakshit S., Mandal A. K., 2019, *MNRAS*, 486, 1781
- Rajput B., Stalin C. S., Sahayanathan S., 2020, *MNRAS*, 498, 5128
- Safna P. Z., Stalin C. S., Rakshit S., Mathew B., 2020, *MNRAS*, 498, 3578
- Sahakyan N., 2020, *A&A*, 635, A25
- Sbarrato T., Ghisellini G., Maraschi L., Colpi M., 2012, *MNRAS*, 421, 1764
- Scarpa R., Falomo R., 1997, *A&A*, 325, 109
- Shah Z., Sahayanathan S., Mankuzhiyil N., Kushwaha P., Misra R., Iqbal N., 2017, *MNRAS*, 470, 3283
- Shakura N. I., Sunyaev R. A., 1973, *A&A*, 24, 337
- Shappee B. J. et al., 2014, *ApJ*, 788, 48
- Shaw M. S. et al., 2012, *ApJ*, 748, 49
- Sikora M., Moderski R., Madejski G. M., 2008, *ApJ*, 675, 71
- Stoeckle J. T., Morris S. L., Gioia I. M., Maccacaro T., Schild R., Wolter A., Fleming T. A., Henry J. P., 1991, *ApJS*, 76, 813
- Thompson D. J. et al., 1995, *ApJS*, 101, 259
- Tramacere A., 2020, Astrophysics Source Code Library, record ascl:2009.001
- Tramacere A., Giommi P., Perri M., Verrecchia F., Tosti G., 2009, *A&A*, 501, 879
- Tramacere A., Massaro E., Taylor A. M., 2011, *ApJ*, 739, 66
- Tripathi T., Devanand P. U., Gupta A. C., Kishore S., Dogra K., Krishna Mohana A., Dhiman V., 2023, *Astron. Telegram*, 15875, 1
- Urry C. M., Mushotzky R. F., 1982, *ApJ*, 253, 38
- Urry C. M., Padovani P., 1995, *PASP*, 107, 803
- Urry C. M., Scarpa R., O'Dowd M., Falomo R., Pesce J. E., Treves A., 2000, *ApJ*, 532, 816
- Vermeulen R. C., Ogle P. M., Tran H. D., Browne I. W. A., Cohen M. H., Readhead A. C. S., Taylor G. B., Goodrich R. W., 1995, *ApJ*, 452, L5
- Wu J., Zhou X., Ma J., Jiang Z., 2011, *MNRAS*, 418, 1640
- Zhang B.-K., Zhou X.-S., Zhao X.-Y., Dai B.-Z., 2015, *Res. Astron. Astrophys.*, 15, 1784

This paper has been typeset from a $\text{\TeX}/\text{\LaTeX}$ file prepared by the author.